McAndrew, A.R., Colegrove, P.A., Addison, A.C., Flipo, B.C.D. and Russell, M.J. 2014. Modelling the influence of the process inputs on the removal of surface contaminants from Ti-6Al-4V linear friction welds. Materials and design, 66(A), pages 183-195. DOI: 10.1016/j.matdes.2014.10.058

Materials and Design 66 (2015) 183–195

Contents lists available at ScienceDirect

Materials and Design

journal homepage: www.elsevier.com/locate/matdes

Modelling the influence of the process inputs on the removal of surface contaminants from Ti–6Al–4V linear friction welds

Anthony R. McAndrew [a,*], Paul A. Colegrove [a], Adrian C. Addison [a], Bertrand C.D. Flipo [b], Michael J. Russell [b]

[a] Cranfield University, Cranfield, Bedfordshire MK43 0AL, UK
[b] TWI Ltd, Granta Park, Great Abington, Cambridge CB21 6AL, UK

ARTICLE INFO

Article history:
Received 28 August 2014
Accepted 24 October 2014
Available online 3 November 2014

Keywords:
Linear friction welding
Additive manufacture
Modelling

ABSTRACT

The linear friction welding (LFW) process is finding increasing interest from industry for the fabrication of near-net-shape, titanium alloy Ti–6Al–4V, aerospace components. Currently, the removal of surface contaminants, such as oxides and foreign particles, from the weld interface into the flash is not fully understood. To address this problem, two-dimensional (2D) computational models were developed using the finite element analysis (FEA) software DEFORM and validated with experiments. The key findings showed that the welds made with higher applied forces required less burn-off to completely remove the surface contaminants from the interface into the flash; the interface temperature increased as the applied force was decreased or the rubbing velocity increased; and the boundary temperature between the rapid flash formation and negligible material flow was approximately 970 °C. An understanding of these phenomena is of particular interest for the industrialisation of near-net-shape titanium alloy aerospace components.

1. Introduction

Linear friction welding (LFW) is a solid-state joining process that is used for the fabrication of near-net-shape, titanium alloy Ti–6Al–4V, aerospace components [1,2]. This is primarily due to the significant cost savings can be achieved when compared to other manufacturing techniques [2,3]. The process also offers many advantages over traditional fusion welding methods [2,3], including excellent mechanical properties, avoidance of melting and very low defect rates.

During LFW one workpiece is oscillated relative to another whilst under a compressive force. Despite being one continuous process, LFW is said to occur over four [4–6] phases:

- Phase 1 – initial phase. Contact exists between asperities on the two surfaces to be joined and heat is generated due to friction – see Fig. 1(a). The asperities soften and deform, increasing the true area of contact between the workpieces. Negligible axial shortening (burn-off) perpendicular to the direction of oscillation is observed during this phase.
- Phase 2 – transition phase. The material plasticises and becomes highly viscous causing the true area of contact to increase to 100% of the cross-sectional area – see Fig. 1(b). The heat conducts back from the interface plasticising more material and the burn-off begins to occur due to viscous material expulsion.
- Phase 3 – equilibrium phase. The interface force, thermal profile and burn-off rate reach a quasi-steady-state condition and significant burn-off occurs through the rapid expulsion of viscous material from the interface.
- Phase 4 – deceleration phase. The relative motion is ceased and the workpieces are aligned. In some applications an additional forging force may also be applied.

Despite the benefits, LFW has experienced limited industrial implementation. One of the reasons for this is due to a lack of fundamental scientific understanding [7]. The rapid nature of the process and the fact that the interface of the workpieces cannot be observed during welding particularly inhibits increased understanding. Computational models offer a pragmatic method to understand what is happening during the rapidly evolving process. Various authors have developed two [1,6–16] and three [15,17–25] dimensional (2D/3D) computational models. These models have been used to predict various weld responses, such as: residual stress formation [11,13], strain rates [1], flash morphology [1,12], flash formation rates [1,8,9,12,19], thermal fields [1,6,8–12,14,17,19–21,25] and microstructural evolution [23]. Although the 2D models do not model the material expulsion perpendicular to the direction of oscillation they do provide a good insight into the process without

* Corresponding author. Tel.: +44 (0)1234 750111 (5055).
E-mail address: a.r.mcandrew@cranfield.ac.uk (A.R. McAndrew).

http://dx.doi.org/10.1016/j.matdes.2014.10.058
0261-3069/

requiring the heavy computational times of the 3D models. According to the reviewed literature, there are three main approaches that may be taken when finite element modelling the LFW process [1,6–25], which are illustrated in Fig. 2.

The first approach [8,13,17,19–21,23,24] involves modelling the two workpieces as individual objects, as shown in Fig. 2(a). This allows the entire process to be modelled. However, the problem with this approach is that the coefficients of friction need to be known so that the thermal aspects of the model during phase 1 can be replicated accurately. Also, models of this type show that the two workpieces never truly merge – as happens in reality for many materials [2,26,27] – meaning that the mechanical mixing of the separate workpieces is not considered. The second approach [7,9,10,14–16,18,22,25] is to model only one workpiece, which is oscillated against a non-deformable surface, as shown in Fig. 2(b). This approach allows for quicker computational times as only half of the geometry is modelled. Many of the problems with this approach are the same as the first. The third approach [1,11,12], as shown in Fig. 2(c), was developed by Turner et al. [1], who noticed that prior to sticking friction taking place there is negligible macroscopic plastic deformation, at least for the titanium alloy Ti–6Al–4V. Once sticking friction begins the process may be modelled as a single body due to there being approximately 100% true interface contact. A temperature profile needs to be mapped onto the single body model to account for the heat generated during sliding friction. The high temperature at the weld interface allows the material at the centre of the model to be highly viscous, thus allowing the single body to represent two individual workpieces. Due to the adhesion of the interface material being modelled this approach considers the mechanical mixing of the separate workpieces and produces much better replications of the flash morphology for Ti–6Al–4V workpieces [1,12]. The limitation of this approach is that the stages prior to sticking friction occurring are not modelled.

Surface contaminants, such as oxides and foreign particles, at the weld interface affect the properties [26,28] and possibly the service life of a weld [1]. Oxides are generated during phase 1 when the hot interface material reacts with the atmosphere [29]. It is also possible that some surface oxides may remain at the interface due to insufficient pre-weld cleaning. The foreign particles may constitute oil or grease from workpiece machining which were also not removed during pre-weld cleaning. At the start of phase 2 the contaminants become trapped at the interface during adhesion of the viscous material. Many authors suggest that a weld is likely to be free from contaminants if all of the initial contacting interface material is expelled into the flash [28,30–32]. Wanjara and Jahazi [26] have shown that for the same burn-off distance, contaminants were present at the interface if lower values of frequency, amplitude and applied force were used, whereas if higher values were used the interface was free from surface contaminants. Therefore surface contaminant removal appears to be critically dependent on the combination of process inputs used. However, the reasons why the process inputs affect surface contaminant removal are not understood. According to Grujicic et al. [23] excessive burn-off to facilitate the removal of the surface contaminants leads to a loss of material and productivity, which ultimately increases industrial costs. Therefore there is an industrial need to understand the mechanisms behind surface contaminant removal to increase safety and reduce costs. Models are able to give an insight into the material expulsion and thus the likelihood of contaminants existing in a real weld [1]. The primary purpose of this paper is to use experimentally validated models to investigate the process input effects on the thermal fields, material flow and surface contaminant removal during the linear friction welding of Ti–6Al–4V workpieces.

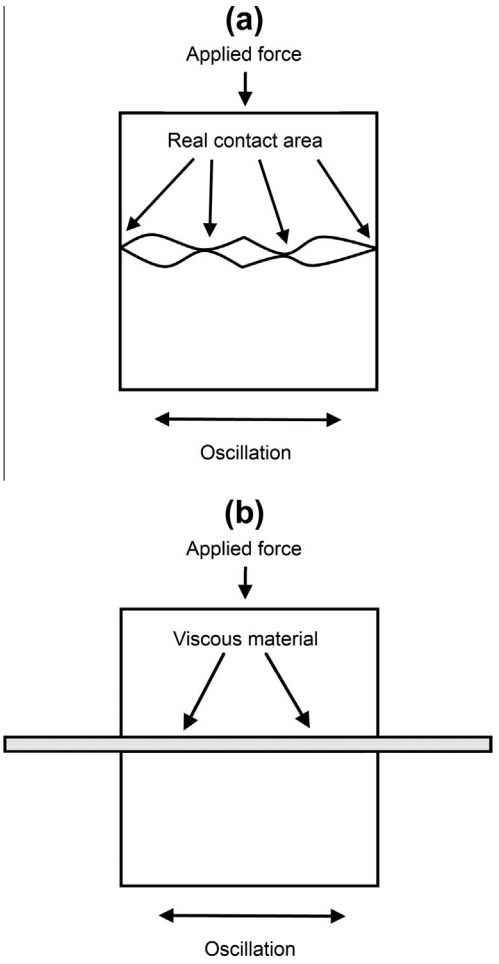

Fig. 1. Key stages of the linear friction welding process: (a) asperity interaction (sliding friction) and (b) viscous material flow (sticking friction).

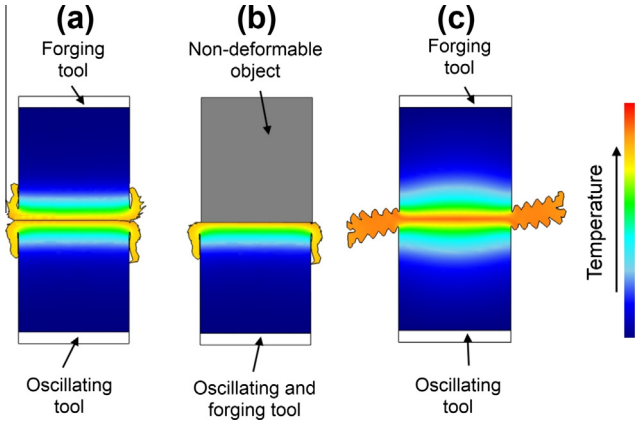

Fig. 2. Modelling approaches: (a) two workpieces, (b) one workpiece and a non-deformable object, and (c) a single body representing two workpieces.

2. Methodology

2.1. Experimental details

Previous work by the authors [6] detailed how Design Expert V.7, a design of experiments (DOE) software package, was used to determine a set of experiments to relate the main process inputs

(amplitude, frequency, applied force and burn-off) to the process outputs, such as the power input, coefficient of friction and interface force generated over a phase for Ti–6Al–4V workpieces with the dimensions shown in Fig. 3(a). The experimental design was specified to include enough design points to account for a quadratic relationship between the inputs and outputs since this behaviour has been observed in the literature [3,26]. Some of the experiments were repeated to test the variance giving 25 experimental conditions for the DOE analysis, which are listed (welds 1–25) in Table 1. This experimental run was also used in this paper.

Four experiments were also completed using thermocouples (welds 26–29). To insert the k-type thermocouples several workpieces had four 1.2 mm diameter holes drilled through them perpendicularly to the oscillation direction and parallel to the direction of the applied force at the positions shown in Fig. 3(b). To position the thermocouples at distances of 0.3 mm, 1 mm, 2.5 mm and 4.5 mm from the weld interface a plug was placed into the holes at the interface end of the workpiece. The thermocouple wire was inserted through the opposite end until it made contact with the plug, the thermocouples where then fixed into position using an epoxy resin.

Finally, a few additional experiments were also completed to investigate how the burn-off affected surface contaminant removal from the interface for the geometry in Fig. 3(a). Four different combinations of frequency, amplitude and applied force were used with burn-off values of 0.5 mm, 1 mm and 3 mm. These combinations are listed (welds 30–41) in Table 1. Unlike the previous experiments [6], these were not cleaned with acetone prior to welding to facilitate clearer observation of the surface contaminant removal in the post weld analysis. All of the detailed experiments; which were completed using the FW34 LFW machine at TWI, Cambridge; were used to provide validation for the models developed in this paper.

Metallographic specimens were produced from experiments 30–41 in Table 1 in accordance with the plane shown in Fig. 3(a), i.e. they were sectioned and polished so that the centre of the weld may be viewed in the direction of oscillation. The sectioned samples were placed into a cold resin and then ground down using the following grit silicon carbide papers: 240, 1200, 2500 and 4000. After grinding the sectioned samples were polished using colloidal silica polish on a micro-cloth and etched using hydrofluoric acid. The metallographic samples were viewed under a refractive microscope to determine the extent of the observable TMAZ at the centre of the weld (i.e. the distance from one TMAZ/parent material boundary to the other) and the thickness of the flash at the point of exit of the weld, as shown in Fig. 4(a) and (b), respectively. Furthermore the samples were also inspected to see if surface contaminants could be observed.

The total energy inputted to the weld interface for a phase, E_x, may be estimated [6,31] by integrating the power with respect to time:

$$E_x = \int_0^T F_{int}\, v dt \tag{1}$$

where T is the total duration of the phase, v is the velocity and F_{int} is the interface force at a specific point in time during a sinusoidal cycle. As with previous work [6], the experimental output data from the FW34 LFW machine was used to determine these values.

To determine the *average* power input generated over a phase, the integrated energy input for that phase was divided by the phase duration. The *average* interface force generated over a phase was also recorded, this allowed for an investigation into the effects of the surface contaminant layer on the flow behaviour of the welds.

2.2. Development of a numerical model

Accurate prediction of the material flow was of primary concern; consequently modelling approach 3, as illustrated in Fig. 2(c), was used. This involved modelling the process as two distinct stages. The first stage used a purely thermal model to replicate the heating of the workpieces during phase 1 and the second stage used a plastic flow model to account for the material flow during phases 2 and 3.

The same design of experiments approach previously reported (welds 1–25 in Table 1) was used for the modelling work in this paper, however, only 16 plastic flow models were required to cover the 25 design points since a single plastic flow model can describe multiple burn-off values for the same combination of frequency, amplitude and applied force. All of the plastic flow models were run to a burn-off of 3 mm and the process history was evaluated at the shorter burn-off values for the design points of interest. The development of the thermal models to account for the phase 1 heating is reported by the authors elsewhere [6] (although the general concepts are discussed in Section 2.2.1).

As previously stated, 3D models require substantially more time to solve than their 2D counterparts: approximately 4 weeks compared to 12 h for the geometry and conditions of interest in

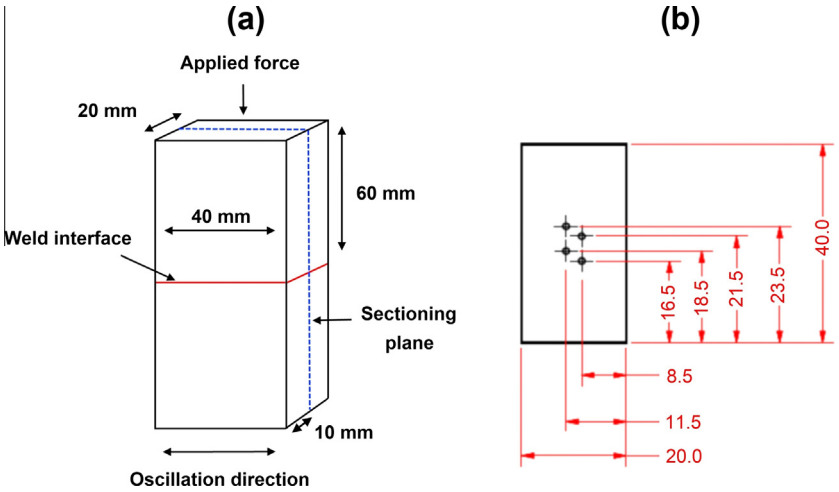

Fig. 3. (a) Experimental workpiece dimensions and location of the sectioning plane (note that 60 mm represents the height of a single workpiece), and (b) thermocouple hole positions (dimensions are in millimetres).

Table 1
Experimental conditions.

Weld	Frequency (Hz)	Amplitude (mm)	Force (kN)	Burn-off (mm)	Purpose
1	50	2.7	66	1	DOE
2	70	1	100	3	DOE
3	20	2.7	100	3	DOE
4	70	1	100	1	DOE
5	58.2	2	32	1	DOE
6	50	2.7	100	2	DOE
7	30	2.7	32	1	DOE
8	60	1.9	100	3	DOE
9	30	2	32	3	DOE
10	50	2.7	32	3	DOE
11	23.3	1.3	77.3	1	DOE
12	20	2.7	100	1	DOE
13	30	1	100	3	DOE
14	20	1.5	100	2	DOE
15	42.3	1.5	68.3	2	DOE
16	31.6	2.3	68.3	2.5	DOE
17	64.1	1.5	66	1	DOE
18	42.1	2.4	32	2	DOE
19	64.1	1.5	66	3	DOE
20	60	1.9	100	1	DOE
21	30	2	32	3	DOE
22	20	2.7	100	1	DOE
23	50	2.7	32	3	DOE
24	20	1.5	100	2	DOE
25	30	1	100	3	DOE
26	20	1.5	100	3	Thermocouple
27	50	2.7	100	3	Thermocouple
28	30	2	32	3	Thermocouple
29	50	2.7	32	3	Thermocouple
30	50	2.7	100	0.5	Burn-off investigation
31	50	2.7	100	1	Burn-off investigation
32	50	2.7	100	3	Burn-off investigation
33	50	2.7	32	0.5	Burn-off investigation
34	50	2.7	32	1	Burn-off investigation
35	50	2.7	32	3	Burn-off investigation
36	20	1.5	100	0.5	Burn-off investigation
37	20	1.5	100	1	Burn-off investigation
38	20	1.5	100	3	Burn-off investigation
39	30	2	32	0.5	Burn-off investigation
40	30	2	32	1	Burn-off investigation
41	30	2	32	3	Burn-off investigation

this paper, see Fig. 3(a) and Table 1. Therefore, to be pragmatic, a 2D modelling approach was used for the 16 conditions required for the DOE analysis. Consequently assumptions had to be made, like neglecting the material expulsion perpendicular to the direction of oscillation. The 2D models were developed with the finite element analysis (FEA) software DEFORM.

2.2.1. Thermal model

Previous work [6] by the authors demonstrated how 2D models can be used to estimate the heating during phase 1 for the workpieces displayed in Fig. 3(a). The 2D model used is displayed in Fig. 5(a). The tooling extended to within 5 mm of the interface as occurred in the experiments. A uniform mesh size of 0.5 mm was used across the model. Temperature dependent thermal conductivity, specific heat and emissivity data from the DEFORM software's library were used. The convective heat transfer coefficient was assumed [1] to be 10 W/(m^2 K); and the conductive heat transfer coefficient with the tooling was assumed [1] to be of 10,000 W/(m^2 K). The temperature of the environment was assumed to be 20 °C.

A uniform heat flux (Q) was applied across most of the workpiece interface which was linearly reduced to 50% of this value from an amplitude (A) away from the edge as shown in Fig. 5. The reduction at the edges was due to the sinusoidal movement of the workpieces – the point at the corner was only in contact with the other workpiece 50% of the time. The heat flux was determined by dividing the process input combination dependent phase 1 power input – see Eq. (2) – by the average in-contact interface area of the workpieces.

$$\begin{aligned}\textbf{\textit{Average phase 1 power}} = {} & -18.26366 + 0.32678 * f \\ & + 9.27832 * A + 0.061476 * F_a \\ & + 0.087638 * f * A - 4.21790 \\ & * 10^{-4} * f * F_a - 2.33759 * 10^{-3} \\ & * f^2 - 1.93524 * A^2 \end{aligned} \quad (2)$$

where: A is the amplitude, f is the frequency and F_a is the applied force.

The interface temperature at the end of phase 1, irrespective of the process inputs, has been shown to reach approximately 1000 °C [6], consequently, the heat flux was applied until the elements at the interface had achieved this temperature. The generic appearance of the thermal profile at the end of phase 1 is shown in Fig. 5(b).

2.2.2. Plastic flow model

The 2D analysis assumed that no material flow occurred perpendicularly to the direction of oscillation. As such, a 2D plane strain condition was used so that the models represented a slice at the centre of the workpieces in Fig. 3(a), with the direction of oscillation being in-plane. As shown in Fig. 6(a), the 2D plastic flow models were specifically designed to focus on the weld interface of

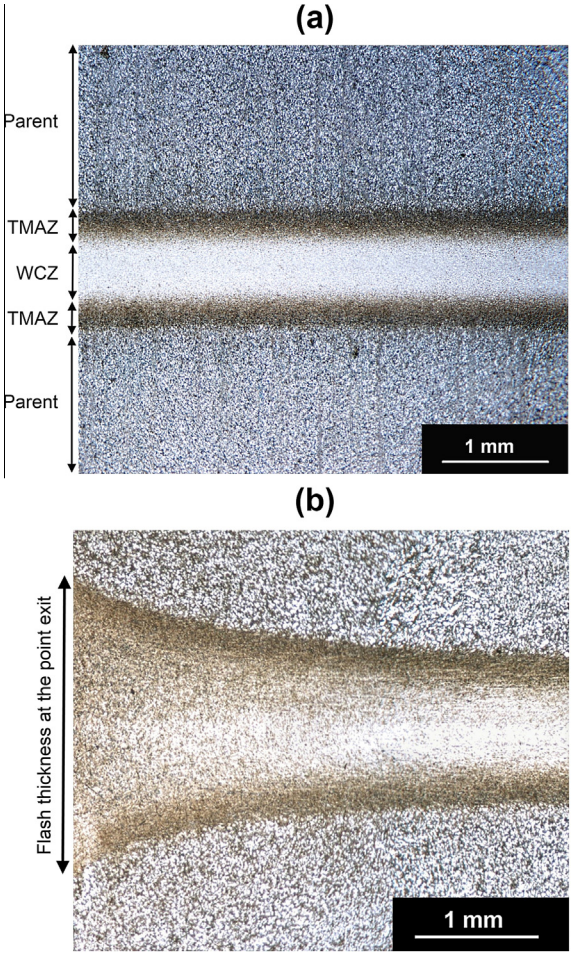

Fig. 4. Experimental responses showing: (a) the weld centre zone (WCZ), the thermo-mechanically affected zone (TMAZ), and the parent material (Parent) [6]; and (b) the flash thickness at the point of exit.

the workpieces to reduce the computational time. The oscillation movement and the applied force were provided by the lower and upper dies, respectively. The thermal profiles at the end of phase 1 from the thermal models were mapped onto the plastic flow models, as illustrated in Fig. 6(b).

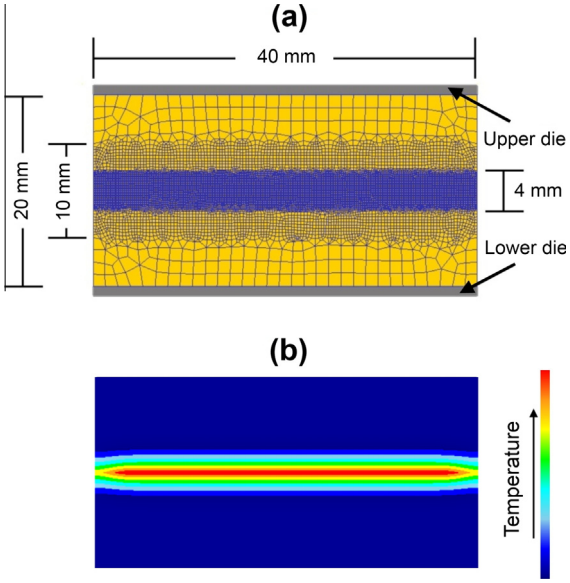

Fig. 6. 2D modelling development showing: (a) plastic flow model setup, (b) plastic flow model with a thermal profile mapped on.

A study on the effects of the mesh element size was performed. It was found that the plastic deformation results were independent of the mesh size for an average element size below 0.13 mm. Due to most of the plastic deformation and heat generation occurring at the interface, most of the mesh elements – with a width of 0.13 mm – were placed in a 4 mm band around the interface, as shown in Fig. 6(a). The relative element size was increased outside of the 4 mm band.

The responses obtained from the modelling will only be as accurate as the input data. As such, the material flow stress data used in this work was the same as that reported by Turner et al. [1]. In summary, the material flow stresses were obtained from stress and strain curves for temperatures, strains and strain rates up to 1500 °C, 4 and 1000 s^{-1}, respectively. The values for the thermal conductivity, specific heat capacity, emissivity, and heat

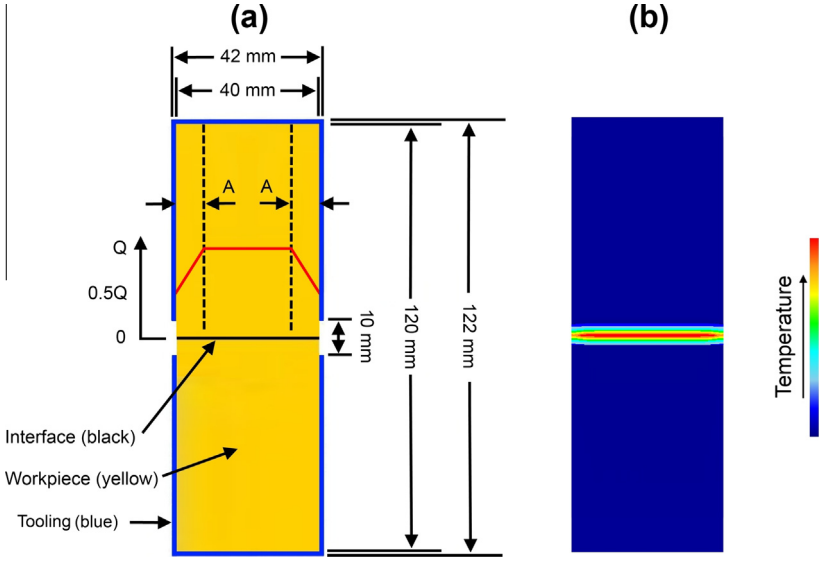

Fig. 5. Developed 2D thermal model showing: (a) the heat flux approach used [6] and (b) an illustration of the generic thermal profile generated at the end of phase 1.

transfer to the tooling and environment were identical to the values used for the thermal models.

Each model was given a time-step so that it approximately travelled a third of the interface mesh element thickness per iteration. The thermal and mechanical aspects of the analysis were coupled and, in accordance with the literature [9,19,20], 90% of the mechanical energy used to deform the material was estimated to be converted into heat. A re-mesh was initiated every 0.1 s for all cases.

Several responses were recorded from the models. To understand the expulsion of the surface contaminants point tracking was used at the interface, with a 1 mm gap between each point, as shown in Fig. 7(a). The models were then run to the desired burn-off and the amount of points that remained recorded. This allowed for an understanding of which combination of process inputs were required to ensure complete expulsion of the point tracking into the flash, as shown in Fig. 7(b). Other responses investigated included: the steady-state burn-off rate, which was calculated by determining the gradient of the line when the burn-off rate is approximately constant; the peak interface temperature; strain rate; extent of the region being strained (TMAZ); the average power input and interface force generated during phase 3; and the flash thickness at the point of exit.

2.3. Regression analysis

An "analysis of variance" (ANOVA) was conducted using Design Expert V.7. This identified which inputs and input interactions were statistically important for mathematically describing the process outputs. The statistically insignificant factors were then removed from the regression analysis equations. This took place for both the results from the FEA and the physical experiments. Several statistical criteria were considered when reducing the factors. These are listed below, and the reader is referred to the cited text for further explanation [33]:

- **R-Squared (R^2)**: The percentage of variation in the data explained by the regression model.
- **Adjusted R-Squared (Adj R^2)**: As for R^2 but adjusted for the number of factors in the model.
- **Predicted R-Squared (Prd R^2)**: A measure of the percentage of variation for new data explained by the model.
- **Adequate Precision (Ad. Pr)**: This is the signal to noise ratio and compares the range of the predicted values at the design points to the average prediction error.

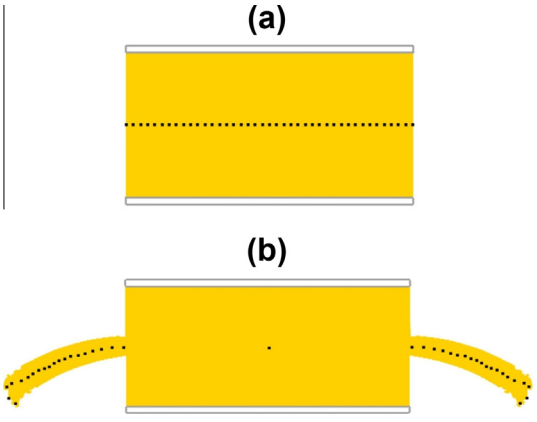

Fig. 7. Recording the FEA responses: (a) interface point tracking and (b) point tracking removed from the interface into the flash (note that there will always be a null flow point at the centre).

- **P-Values (P-V)**: This helps the user determine which input factors are of significance. The smaller the value the better, with values equal to or lower than 0.05 being statistically significant. The overall value for the equation describes how significant it is.

3. Results and discussion

3.1. Regression analysis

The results from the statistical tests performed on the final regression analysis equations for the FEA and experiments are displayed in Table 2, where Av. and EXP represent *average* and *experiment*, respectively. Much of the variability within the results is accounted for due to many of the values being close to 100%. These results are presented first as the following discussions integrate the FEA and experimental results.

The equations for the completed regression analysis are listed below:

$$\textbf{\textit{Burn}} - \textbf{\textit{off rate}}(\textbf{\textit{FEA}}) = -1.36198 - 0.032022 * f + 1.30674 * A - 1.90035 * 10^{-3} * F_a + 0.028506 * f * A + 3.87983 * 10^{-4} * f * F_a + 2.69099 * 10^{-3} * A * F_a - 0.32656 * A^2 \quad (3)$$

$$\textbf{\textit{Burn}} - \textbf{\textit{off rate}}(\textbf{\textit{EXP}}) = 0.69581 - 0.042711 * f + 0.039751 * A - 6.79114 * 10^{-3} * F_a + 0.036051 * f * A + 4.66901 * 10^{-4} * f * F_a \quad (4)$$

$$\textbf{\textit{TMAZ thickness}}(\textbf{\textit{FEA}}) = 3.06495 + 1.17408 * A - 0.040652 * F_a - 0.29568 * A^2 + 2.20636 * 10^{-4} * F_a^2 \quad (5)$$

$$\textbf{\textit{Flash thickness}}(\textbf{\textit{FEA}}) = 5.56032 - 3.84187 * 10^{-3} * f - 0.094892 * A - 0.049387 * F_a + 2.80758 * 10^{-4} * F_a^2 \quad (6)$$

$$\textbf{\textit{Interface temperature}}(\textbf{\textit{FEA}}) = 676.29677 + 6.21345 * f + 301.4961 * A - 0.40508 * F_a - 6.71761 * 10^{-3} * f * F_a - 0.57031 * A * F_a - 0.02614 * f^2 - 46.9745 * A^2 + 7.40249 * 10^{-3} * F_a^2 \quad (7)$$

$$\textbf{\textit{Interface strainrate}}(\textbf{\textit{FEA}}) = 53.01137 - 2.18777 * f - 56.11051 * A - 0.34278 * F_a + 5.55938 * f * A + 0.04545 * f * F_a + 0.99927 * A * F_a - 0.015 * F_a^2 \quad (8)$$

$$\textbf{\textit{Remaining point tracking}}(\textbf{\textit{FEA}}) = 31.54378 - 0.48038 * f + 0.088584 * A - 0.061352 * F_a - 13.51208 * B_o + 0.043083 * f * A + 6.99114 * 10^{-4} * f * F_a - 0.019211 * A * F_a + 0.022378 * F_a * B_o + 3.75413 * 10^{-3} * f^2 + 2.10029 * B_o^2 \quad (9)$$

$$\textbf{\textit{Av.phase 3 interface force}}(\textbf{\textit{FEA}}) = 36.63998 - 0.12187 * f - 16.69319 * A + 0.29955 * F_a + 3.81874 * A^2 - 1.63274 * 10^{-3} * F_a^2 \quad (10)$$

$$\textbf{\textit{Av.phase 3 interface force}}(\textbf{\textit{EXP}}) = 55.71070 - 0.63561 * f - 6.22698 * A - 0.016212 * F_a + 0.10859 * f * A + 0.032661 * A * F_a + 5.10434 * 10^{-3} * f^2 \quad (11)$$

$$\textbf{\textit{Av.phase 3 power}}(\textbf{\textit{FEA}}) = -5.04395 - 3.26455 * 10^{-3} * f - 0.050195 * A + 0.16786 * F_a + 0.095837 * f * A - 9.8577 * 10^{-4} * F_a^2 \quad (12)$$

$$\textbf{\textit{Av.phase 3 power}}(\textbf{\textit{EXP}}) = 6.21627 - 0.083060 * f - 2.22581 * A - 0.057055 * F_a + 0.16352 * f * A + 6.46109 * 10^{-4} * f * F_a + 0.025004 * A * F_a \quad (13)$$

where: A is the amplitude, f the frequency, F_a the applied force, and B_o the burn-off.

Table 2
Statistical tests performed on the final regression analysis models.

Process output	R^2 (%)	Adj. R^2 (%)	Prd. R^2 (%)	Ad. Pr.	P-V
Burn-off rate (FEA)	99.8	99.7	99.6	125.9	<0.0001
Burn-off rate (EXP)	93.4	91.7	88.4	23.4	<0.0001
TMAZ thickness (FEA)	92.1	90.5	87.8	19.2	<0.0001
Flash thickness (FEA)	94.8	93.8	91.9	24.1	<0.0001
Interface temperature (FEA)	99.8	99.6	99.3	88.1	<0.0001
Interface strain rate (FEA)	99.7	99.6	99.3	90.3	<0.0001
Remaining point tracking (FEA)	99.1	98.4	97.0	36.8	<0.0001
Av. phase 3 interface force (FEA)	96.0	95.0	93.8	30.8	<0.0001
Av. phase 3 interface force (EXP)	89.9	86.6	82.0	16.2	<0.0001
Av. phase 3 power input (FEA)	98.2	97.7	96.7	41.4	<0.0001
Av. phase 3 power input (EXP)	99.6	99.5	99.2	89.6	<0.0001

With the exception of the point tracking evolution described by Eq. (9), the burn-off, B_o, had no effect on any of the responses. This is in good agreement with other authors who have shown that once Ti–6Al–4V is in the steady-state phase (phase 3) the plastic deformations [1,4,34] and thermal profiles [1,9,15] are independent of the burn-off.

All of the regression analysis plots from this point onward – unless otherwise stated – display the results from the mathematical equations (Eqs. (3)–(13)) as opposed to the actual values recorded from the models and experimental welds. This allowed for a greater understanding of the relationships between the inputs and outputs. Experimental and modelling results are compared where possible.

3.1.1. Mechanisms behind flash formation

The regression analysis demonstrated that it was acceptable to consider the frequency and amplitude of oscillation as a combined single input term called the average rubbing velocity, v_r, which Addison [3] defined as:

$$v_r = 4 \cdot A \cdot f \tag{14}$$

Varying the frequency or amplitude while keeping the average rubbing velocity constant had relatively little effect on the outputs (although this observation may only be applicable to Ti–6Al–4V for the frequency and amplitude range investigated). To illustrate this, the steady state burn-off rates determined from the models and experiments are plotted as a function of the frequency and average rubbing velocity in Fig. 8(a). Therefore all subsequent regression analysis plots are displayed as a function of the average rubbing velocity.

The FEA demonstrated how the flash was generated in the direction of oscillation. When the amplitude was at maximum displacement the in-contact surface area was decreased. This caused a pressure increase, resulting in the cooler material being plunged further into the highly viscous material. As the workpieces were brought back together the cooler material ploughed the viscous material from the interface generating the flash. Fig. 8(b) shows how the burn-off rate (flash formation rate) was affected by the combination of rubbing velocity and applied force used – it increased with both. This phenomenon was due to the increased rubbing velocity causing a faster rate of ploughing; and the increased force causing the cooler material to be plunged even further into the viscous material, resulting in a greater amount of material being ploughed from the interface with each oscillatory cycle, thus increasing the burn-off rate.

As shown in Fig. 8, the models under-predicted the burn-off rate. Turner et al. [1] noticed that there are two mechanisms for expelling the viscous material. The first is the effect of the oscillatory motion pushing and dragging the material out of the weld in the direction of oscillation; the second is the applied force extruding the material in the direction perpendicular to oscillation. The mechanism that dominates depends on the process inputs used. 2D models cannot account for the material being expelled perpendicular to oscillation thus explaining the observed under-prediction. The difference between the experimental and modelled burn-off rates is greatest for low applied forces. This may indicate that under lower applied

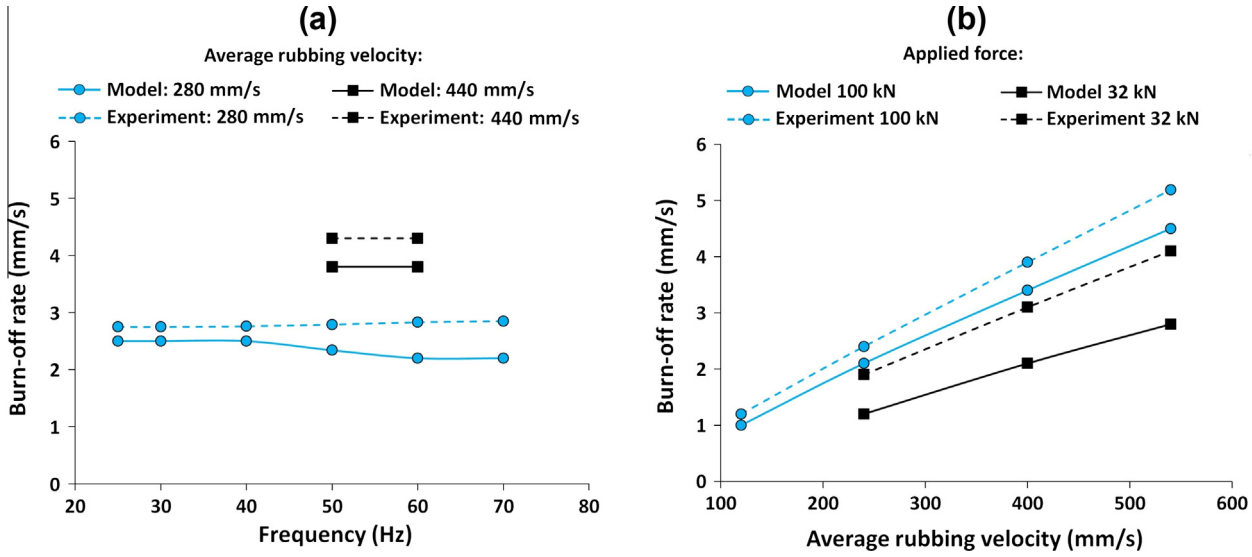

Fig. 8. Regression analysis for the FEA and experimental steady-state burn-off rate: (a) as a function of the frequency and average rubbing velocity for an applied force of 100 kN, and (b) as a function of the average rubbing velocity and applied force.

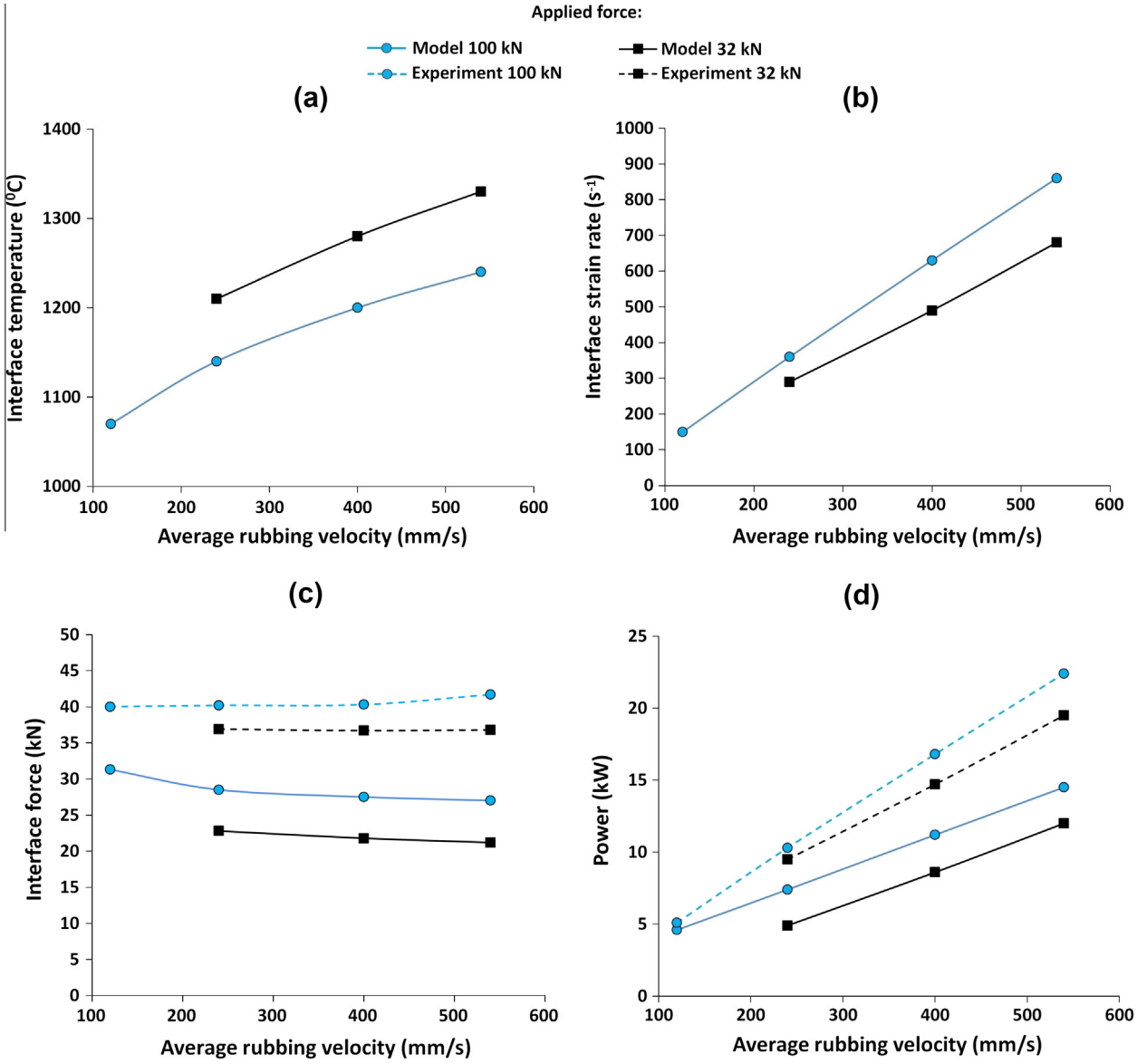

Fig. 9. Regression analysis results for the FEA and experiments for the: (a) peak interface temperature, (b) peak interface strain rate, (c) average interface force during phase 3, and (d) average power input during phase 3.

forces a greater percentage of the material is extruded perpendicular to the direction of oscillation. 3D modelling may provide better insight into this phenomenon.

3.1.2. Energy usage, thermal fields and microstructure

The results from the regression analysis for the peak interface temperature, peak interface strain rate, average interface force generated during phase 3 and the average power input generated during phase 3 are displayed in Fig. 9(a)–(d), respectively.

The average interface force generated over a phase was relatively insensitive to the rubbing velocity (see Fig. 9(c)). This can be explained by the effects of the temperature and strain rate on the flow stress. The interface strain rate increased with the average rubbing velocity (see Fig. 9(b)), which increased the required flow stress [1,35]. However, the higher rubbing velocities also generated a greater heat input (see Fig. 9(d)), which due to the relatively low thermal conductivity of titanium alloys [36] concentrated the heat close to the weld interface. The concentrated heat increased the interface temperature (see Fig. 9(a)) thus reducing the required flow stress [1,35,37]. The net result appears to be a cancellation of the two effects.

As shown in Fig. 9(a), the interface temperature increases as the applied force is *decreased*. This observation was also made by Romero et al. [38] and Turner et al. [11]. This phenomenon can be explained by the relationship between the power input and the burn-off rate. For a comparable rubbing velocity, a reduction in the force resulted in the burn-off rate being reduced by a greater percentage than the power input, as can be seen by comparing Figs. 8(b) and 9(d). Although less heat went into the weld it was not expelled as fast. This increased the time the heat had to conduct back from the interface, thus increasing the size of the band of heated material – see the 540 mm/s profiles in Fig. 10(a). Consequently, the material farther back from the interface was much hotter with lower applied forces. When this hotter material reached the interface its heat combined with the heat generated during the oscillatory motion thus producing a higher interface temperature.

The higher interface temperature would explain why the average interface force generated over a phase decreased as the applied

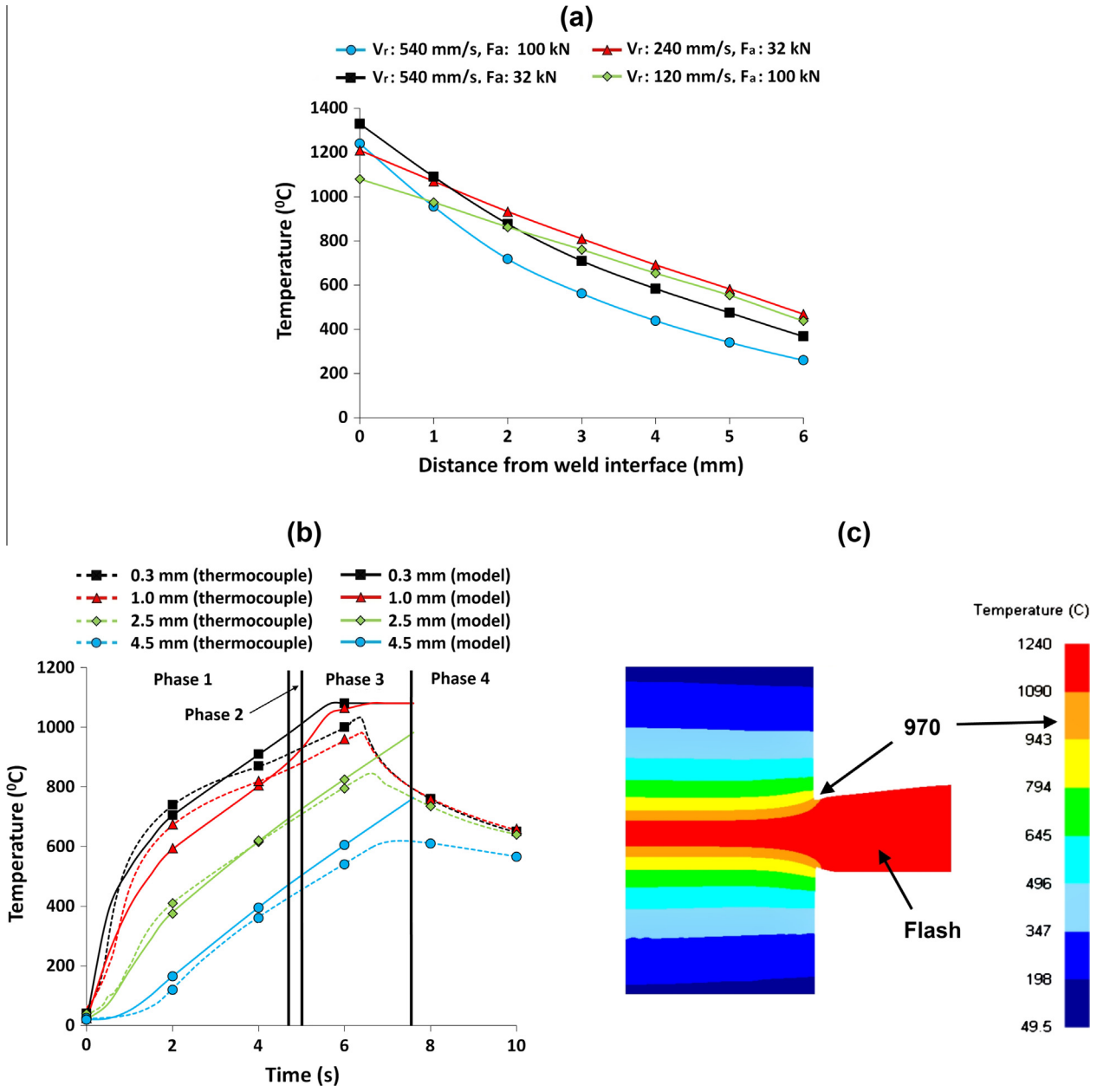

Fig. 10. Thermal histories from the FEA and experiments showing: (a) the effects of different average rubbing velocities, V_r, and applied forces, F_a, on the generated FEA thermal profiles during phase 3; (b) a comparison of the thermal histories between a model and an experiment for the different phases for a frequency, amplitude, applied force and burn-off of 20 Hz, 1.5 mm, 100 kN and 3 mm, respectively (note the distances in the key represent how far back from the interface the recorded points were at the beginning of the process); and (c) FEA boundary temperature between flash formation and negligible material flow.

force was reduced (see Fig. 9(c)), the interface was hotter thus requiring a lower force to maintain oscillatory motion due to the reduction in the required flow stress [1,35,37]. The lower interface force would also explain why the peak strain rate and power input to maintain the steady-state condition were reduced with lower applied forces, as shown in Fig. 9(b) and (d).

The models under-predicted the average interface forces and power inputs, as shown in Fig. 9(c) and (d). This was probably due to two main factors: First, the models did not account for the heat that was expelled into the flash in the direction perpendicular to oscillation. This may have resulted in the modelled weld being comparably hotter than the experimental one. Consequently the models may have had a higher interface temperature, thus requiring a lower force to maintain oscillatory motion; the lower force would have also reduced the power input. The second factor was due to the difference between the flow stress values of the experimental weld and the modelled weld.

As shown in Fig. 10(b), there is a good match between the purely thermal models and thermocouple recordings for the heating during the initial phase (phase 1) of the process. The reason there was disagreement between the thermocouple recordings and the plastic flow models (phases 2 and 3), particularly for the thermocouples initially closest to the interface, was probably due to the same problem encountered by Vairis and Frost [10]. The viscous plasticised material entered the thermocouple hole and pushed the thermocouple back from the interface causing it to record a lower value at an unknown distance farther back. This would explain why there was good initial agreement and then a drop off in the thermocouple recording. This problem was observed for all comparisons between the models and thermocouple trials. As

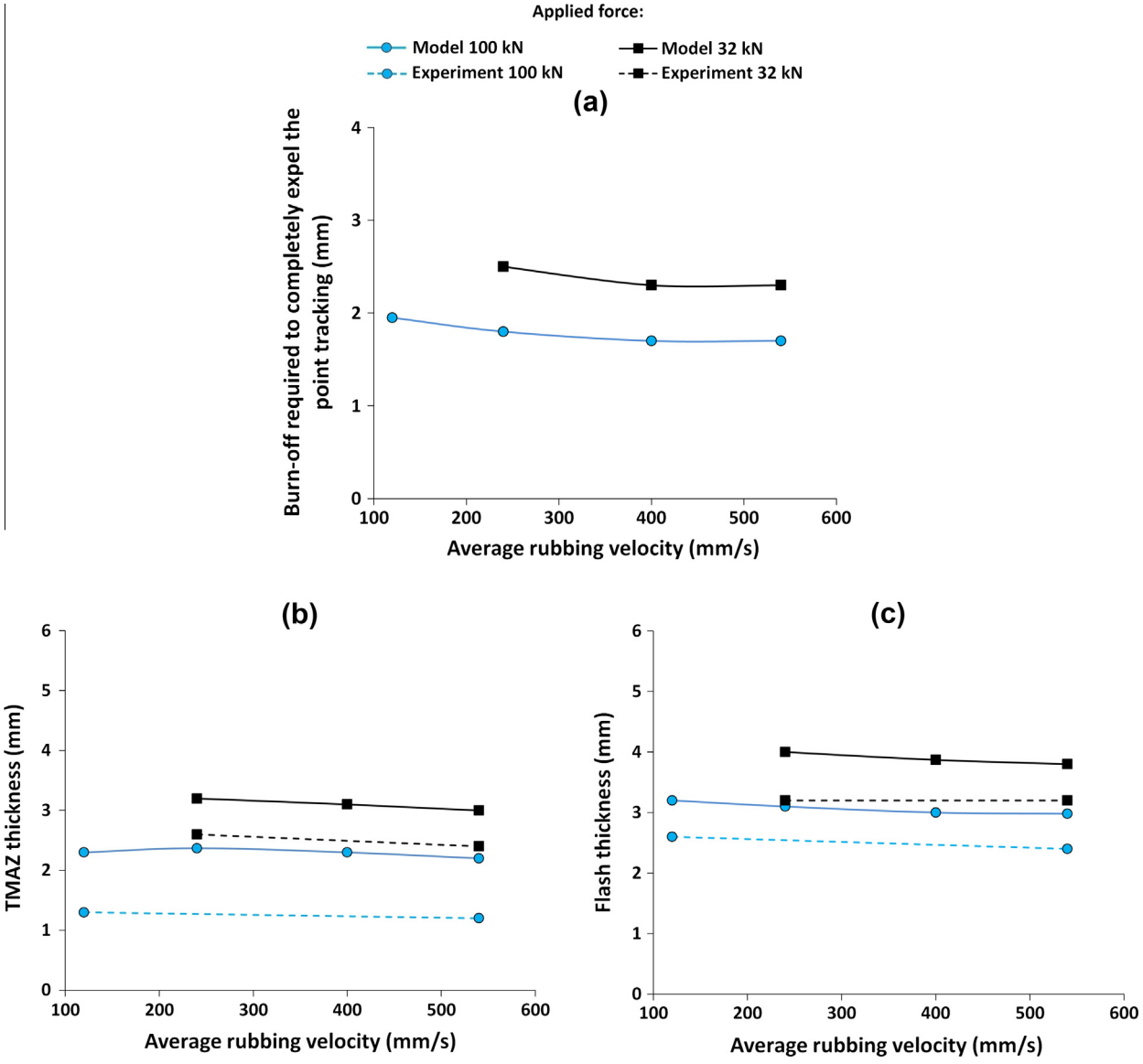

Fig. 11. Regression analysis results for the FEA for the: (a) combination of process inputs required to completely expel the point tracking into the flash, (b) TMAZ thickness, and (c) flash thickness. Note that the experimental flash and TMAZ thicknesses were obtained from the experiments rather than being outputs from a regression model.

previously discussed, there also could have been extra heat in the plastic models due to no flash being expelled perpendicular to the direction of oscillation. This would explain why the peak thermocouple recordings were lower than those of the models. Despite the differences between the models' temperature output and thermocouple recordings during phases 2 and 3, the modelling results are believed to be reasonably accurate due to the weld line temperatures observed in this work (see Fig. 9(a)) being in good agreement with other authors for Ti–6Al–4V, i.e. between 1000 °C and 1300 °C [1,11,12,14,20].

The experimental Ti–6Al–4V workpiece material experienced significant microstructural changes around the interface region. As and shown in Fig. 4(a) and reported previously [6], regardless of the process inputs used, the macrostructures of the Ti–6Al–4V linear friction welds were similar in appearance in the fact that they had several distinct zones – a weld centre zone (WCZ), a thermo-mechanically affected zone (TMAZ) and the parent material. In agreement with Romero et al. [38] and Li et al. [39] it was difficult to detect a purely heat affected zone (HAZ). The microstructural features of the WCZ and TMAZ are summarised below:

- Weld centre zone. The temperature measurements from the models (see Fig. 9(a)) indicated that the WCZ exceeded the beta-transus temperature. The large strains and strain rates in the WCZ (see Fig. 9(b)) induced dynamic recrystallisation of the beta-phase [40,41]. The body-centred-cubic (BCC) beta-phase microstructure [36,42] present at the WCZ during processing had more slip-systems than the hexagonal-close-packed (HCP) alpha-phase [43] and required a lower activation energy to initiate material flow [44,45]. This would explain why the commencement of material flow during the LFW of Ti–6Al–4V is associated with the beta-transus temperature, as previously reported [6]. Depending on the rate of post oscillatory motion cooling [46] the beta-phase at the WCZ transformed into either a Widmanstatten or Martensitic microstructure [6].
- Thermo-mechanically affected zone. The material in this region was affected by the heat and deformed mechanically but there was little evidence that the TMAZ experienced temperatures equal to or greater than the beta-transus or experienced dynamic recrystallization; this was due to the original

alpha-grains of the parent material being present. In agreement with the literature [26,47] many of the TMAZ grains were deformed, elongated and re-orientated in the direction of oscillation.

To obtain a greater insight into the effects of the process inputs on the microstructural evolution during processing, future modelling work could consider combining the parametric approach used in this work with the general methodology for predicting weld microstructural changes reported by Grujicic et al. [23].

Worthy of note, the modelling work in this paper showed that the boundary temperature between the flash formation and negligible material flow was 970 °C (±20 °C), approximately corresponding to the beta-transus temperature, as shown in Fig. 10(c).

3.1.3. Surface contaminant removal

The results from the regression analysis for the combination of process inputs required to completely expel the point tracking into the flash, the TMAZ thickness and the flash thickness are displayed in Fig. 11(a)–(c), respectively. Note that: the burn-off values presented in Fig. 11(a) are the minimum values – according to Eq. (9) – required to ensure fewer than two "tracked points" remained at the interface, i.e. the minimum burn-off required so that only the null flow point was present; and the experimental flash and TMAZ thicknesses were physical experimental recordings rather than values estimated by regression analysis equations.

As shown in Fig. 11(a), when the applied force is increased the required burn-off to completely expel the point tracking into the flash decreases. This was due to the influence of the applied force on the generated thermal profiles. As discussed in Section 3.1.2, for the rubbing velocity range investigated the higher forces generated a thinner band of highly heated viscous material (greater than 970 °C). As the size of the band of highly heated material was reduced so was the amount of material required to be expelled along with the point tracking, thus reducing the required burn-off. Despite the large influence the rubbing velocity had on the gradient of the thermal profiles, for a comparable applied force a change in the rubbing velocity had relatively little effect on the extent of the band of material above 970 °C, as shown in Fig. 10(a). Consequently, the rubbing velocity had relatively little effect on the required burn-off to expel the point tracking for the conditions evaluated in this work.

As shown in Fig. 12, there is good agreement between the expulsion of the surface contaminants (the dark clusters along the interface as shown in Fig. 12(a), (b) and (d)) in the experimental welds and the point tracking results from the FEA; both show that the contaminants and point tracking are increasingly expelled toward the edges of the workpieces as more burn-off occurs. For the experiments it became increasingly difficult to optically observe the surface contaminants as the burn-off increased. This was to be expected as the contaminants would have been expelled into the flash and/or heavily strained, thus dispersing them thinly across the weld.

Although there was good agreement between the experiments and FEA for the contaminant evolution during phases 2 and 3, further justification of the assumption that point tracking can effectively represent the contaminants is required. Contaminants may affect the constitutive behaviour of the viscous interface layer, however due to their small size (see Fig. 12(a)) relative to the extent of the flowing material (see Fig. 11(b and c)) their effect is likely to be limited. To justify this view the LFW machine output data was interrogated for the DOE welds that had experienced 3 mm of burn-off (see Table 1). The average interface force between 0 mm and 1 mm of burn-off (where a heavy contaminant presence was expected, see Fig. 12 and previous work [6]) was compared to the average interface force between 1.5 mm and 3 mm (where there was a negligible contaminant presence, see Fig. 12(f)). The analyses showed that the average interface force between the two burn-off regimes typically varied by 3.8% – a minimal difference. The slightly larger forces at the lower burn-off values were more likely to be due to the inclusion of the transition phase (phase 2) than the contaminants – the lower temperature viscous material in the transition phase typically requires a larger force to maintain oscillatory motion [4,6,31]. Therefore the surface contaminants are likely to have had a negligible effect on the overall constitutive behaviour of the viscous interface layer. Consequently FEA used in conjunction with point tracking offers a pragmatic method for understanding the mechanisms behind surface contaminant removal during phases 2 and 3.

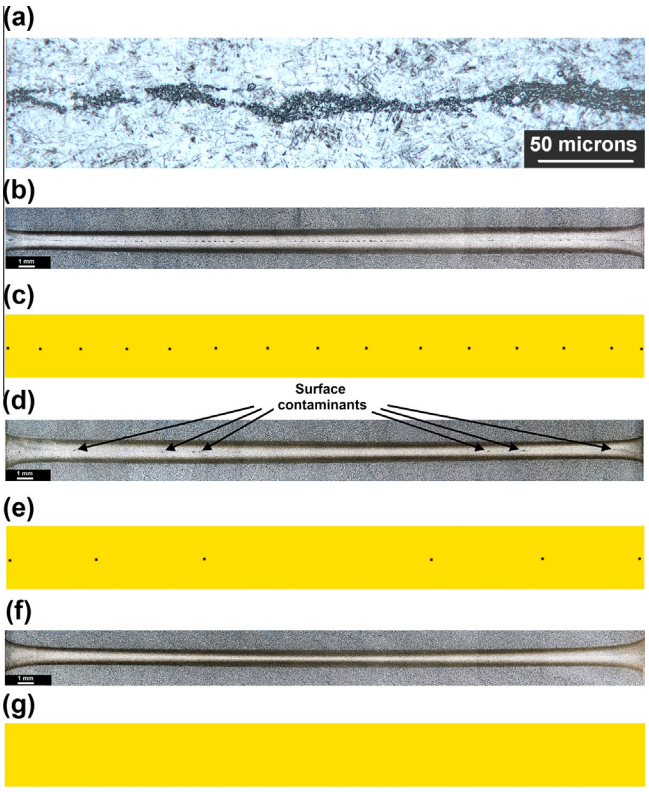

Fig. 12. (a) High magnification of the contaminants present at the weld interface in weld number 11 [6]; and surface contaminant expulsion for an average rubbing velocity of 540 mm/s and an applied force of 100 kN for a burn-off of: (b) 0.5 mm (experiment) and (c) associated FEA, (d) 1 mm (experiment) and (e) associated FEA, (f) 3 mm (experiment) and (g) associated FEA. Note that the null flow point was removed for clarity from (e) and (g).

Furthermore, to investigate the effects of the contaminants during phase 1 on the experimental workpieces the authors compared the average force histories between pre-weld cleaned and non-pre-weld cleaned welds that were run at the same frequency, amplitude and applied force, i.e. weld 6 and weld 30; weld 10 and weld 33; weld 14 and weld 36; and weld 9 and 39 – as detailed in Table 1. The pre-weld cleaned workpieces should have had far less contaminants. The analyses showed no noticeable difference between the average force histories during phase 1; therefore the impact of contaminants during phase 1 also appeared to be small.

Due to a thinner band of highly heated material being produced in welds with higher applied forces the thickness of the flash and the TMAZ are reduced under these conditions, as shown in Fig. 11(b) and (c). An increase of the rubbing velocity had minimal effect on these values. The trends of the flash and TMAZ thickness were captured by the models; however the exact values did not match with the experimental welds. The extra heat in the models (as previously

discussed) and the difference between the experimental and modelling material flow stress data may have contributed to the discrepancies. The experimental welds had also experienced extra material expulsion due to the forging force during phase 4, which may have reduced the values. In addition for the TMAZ thickness results: for the models, the distance between the points of negligible strain either side of the interface were recorded, while in the experimental welds the final observable TMAZ thickness was recorded, which may not have coincided with negligible strain.

4. Conclusions

The following conclusions can be made from this work:

(1) The 2D models gave an insight into the process fundamentals for the LFW of Ti–6Al–4V workpieces. Although the 2D models assumed no material expulsion perpendicularly to the direction of oscillation they still managed to capture the experimental trends.
(2) The measurements from the finite element analysis and the experimental microstructural observations suggest that the weld interface exceeded the beta-transus temperature and experienced dynamic recrystallisation.
(3) The finite element analysis demonstrated that the boundary temperature between the rapid flash formation and negligible material flow was approximately 970 °C.
(4) Finite element analysis used in conjunction with point tracking was an effective way to evaluate surface contaminant removal.
(5) The surface contaminants were increasingly expelled from the weld interface as the burn-off was increased.
(6) An increase of the applied force increased the steady-state burn-off rate, interface strain rate, power input and interface force; whilst decreasing the interface temperature, flash thickness, TMAZ thickness, and the overall burn-off required to expel the point tracking/surface contaminants.
(7) An increase of the average rubbing velocity increased the interface temperature, strain rate, steady-state burn-off rate and power input; whilst having relatively little influence on the flash thickness, TMAZ thickness and the overall burn-off required to expel the point tracking/surface contaminants.
(8) For the process input combinations investigated it may be advantageous to produce Ti–6Al–4V linear friction welds using higher applied forces. This is because the material consumption to remove the surface contaminants will be reduced, thus increasing the safety factor for a set burn-off value.

Acknowledgements

The authors would like to thank the Engineering and Physical Sciences Research Council (EPSRC), The Boeing Company and The Welding Institute (TWI) for funding the research presented in this paper. Also, the advice provided by Dr. Richard Turner of the University of Birmingham, Mr. James Farrar of Wilde Analysis Ltd. and Mr. David Bolser of The Boeing Company was greatly appreciated.

References

[1] Turner R, Gebelin J-C, Ward RM, Reed RC. Linear friction welding of Ti–6Al–4V: modelling and validation. Acta Mater 2011;59:3792–803.
[2] Addison AC. Linear Friction Welding of Engineering Metals. TWI Industrial Members Report – 894/2008. Cambridge, U.K.: 2008.
[3] Addison AC. Linear friction welding information for production engineering. TWI Industrial Members Report – 961/2010. Cambridge, U.K.: 2010.
[4] Vairis A, Frost M. High frequency linear friction welding of a titanium alloy. Wear 1998;217:117–31.
[5] Vairis A, Frost M. On the extrusion stage of linear friction welding of Ti 6Al 4V. Mater Sci Eng A 1999;271:477–84.
[6] McAndrew AR, Colegrove PA, Flipo BCD, Addison AC, Russell MJ. Energy and force analysis of Ti–6Al–4V linear friction welds for computational modeling input and validation data. Metall Mater Trans A 2014;45:6118–28.
[7] Li W, Suo J, Ma T, Feng Y, Kim K. Abnormal microstructure in the weld zone of linear friction welded Ti–6.5Al–3.5Mo–1.5Zr–0.3Si titanium alloy joint and its influence on joint properties. Mater Sci Eng, A 2014;599:38–45.
[8] Ceretti E, Fratini L, Giardini C, Spisa D. Numerical modelling of the linear friction welding process. IntJ Mater Form 2010;3:1015–8.
[9] Li W, Ma T, Li J. Numerical simulation of linear friction welding of titanium alloy: effects of processing parameters. Mater Des 2010;31:1497–507.
[10] Vairis A, Frost M. Modelling the linear friction welding of titanium blocks. Mater Sci Eng A 2000;292:8–17.
[11] Turner R, Ward RM, March R, Reed RC. The magnitude and origin of residual stress in Ti–6Al–4V linear friction welds: an investigation by validated numerical modeling. Metall. Mater Trans B 2012;43:186–97.
[12] Schroeder F, Ward RM, Turner RP, Attallah MM, Gebelin J, Reed RC. Linear friction welding of titanium alloys for aeroengine applications : modelling and Validation. In: 9th International Conference on Trends in Welding Research, Chicago, U.S.A; 2012, p. 886–892.
[13] Song X, Xie M, Hofmann F, Jun TS, Connolley T, Reinhard C, et al. Residual stresses in linear friction welding of aluminium alloys. Mater Des 2013;50:360–9.
[14] Li W, Shi SX, Wang FF, Ma TJ, Li JL, Gao DL, et al. Heat reflux in flash and its effect on joint temperature history during linear friction welding of steel. Int J Therm Sci 2013;67:192–9.
[15] Li W, Wang F, Shi S, Ma T. Numerical simulation of linear friction welding Based on ABAQUS environment: challenges and perspectives. J Mater Eng Perform 2014;23:384–90.
[16] Zhao P, Fu L, Zhong D. Numerical simulation of transient temperature and axial deformation during linear friction welding between TC11 and TC17 titanium alloys. Comput Mater Sci 2014;92:325–33.
[17] Fratini L, Buffa G, Campanella D, La Spisa D. Investigations on the linear friction welding process through numerical simulations and experiments. Mater Des 2012;40:285–91.
[18] Liu ZM, Guo ZU, Zhao GY, Zhang S, Pan JL. 3D Numerical simulation of linear friction welding of 45# carbon steel. Adv Mater Res 2012;538–541:1443–6.
[19] Sorina-Müller J, Rettenmayr M, Schneefeld D, Roder O, Fried W. FEM simulation of the linear friction welding of titanium alloys. Comput Mater Sci 2010;48:749–58.
[20] Grujicic M, Arakere G, Pandurangan B, Yen CF, Cheeseman BA. Process modeling of Ti–6Al–4V linear friction welding (LFW). J Mater Eng Perform 2011;21:2011–23.
[21] Wu X. Finite element simulation of linear friction welding. Adv Mater Res 2012;411:126–9.
[22] Li W, Wang F, Shi S, Ma T, Li J, Vairis A. 3D finite element analysis of the effect of process parameters on linear friction welding of mild steel. J Mater Eng Perform 2014;23:4010–8.
[23] Grujicic M, Yavari R, Snipes JS, Ramaswami S, Yen C-F, Cheeseman BA. Linear friction welding process model for carpenter custom 465 precipitation-hardened martensitic stainless steel. J Mater Eng Perform 2014;23:2182–98.
[24] Vaziri M, Berg S, Sandberg D, Gheinani IT. Three-dimensional finite element modelling of heat transfer for linear friction welding of Scots pine. Wood Mat Sci Eng 2014:1–8.
[25] Tao J, Zhang T, Liu P, Li J, Mang Y. Numerical computation of a linear friction welding process. Mater Sci Forum 2008;575–578:811–5.
[26] Wanjara P, Jahazi M. Linear friction welding of Ti–6Al–4V: processing, microstructure, and mechanical-property inter-relationships. Metall Mater Trans A 2005;36:2149–64.
[27] Lang B, Zhang TC, Li XH, Guo DL. Microstructural evolution of a TC11 titanium alloy during linear friction welding. J Mater Sci 2010;45:6218–24.
[28] Chamanfar A, Jahazi M, Gholipour J, Wanjara P, Yue S. Maximizing the integrity of linear friction welded Waspaloy. Mater Sci Eng A 2012;555:117–30.
[29] Stachowiak GW, Batchelor AW. Engineering tribology. 2nd ed. Oxford, U.K.: Butterworth-Heinemann; 2000.
[30] Bhamji I, Preuss M, Threadgill PL, Addison AC. Solid state joining of metals by linear friction welding: a literature review. Mater Sci Technol 2011;27:2–12.
[31] Ofem UU, Colegrove PA, Addison A, Russell MJ. Energy and force analysis of linear friction welds in medium carbon steel. Sci Technol Weld Joining 2010;15:479–85.
[32] Vairis A, Christakis N. The development of a continuum framework for friction welding processes with the aid of micro-mechanical parameterisations. Int J Model Identif Contr 2007;2:347–55.
[33] Montgomery DC. Design and analysis of experiments. 5th ed. New York, NY: John Wiley and Sons, inc; 2000.
[34] Vairis A. Mathematical modelling of the linear friction welding process. J Eng Sci Technol Rev 2012;5:25–31.
[35] Seshacharyulu T, Medeiros SC, Frazier WG, Prasad YVRK. Hot working of commercial Ti–6Al–4V with an equiaxed a – b microstructure: materials modeling considerations. Mater Sci Eng A 2000;284:184–94.
[36] Leyens C, Peters M. Titanium and titanium alloys: fundamentals and applications. 1st ed. Darmstadt: Wiley-VCH; 2003.

[37] Lee W, Lin C. High-temperature deformation behaviour of Ti6Al4V alloy evaluated by high strain-rate compression tests. J Mater Process Technol 1998;75:127–36.
[38] Romero J, Attallah MM, Preuss M, Karadge M, Bray SE. Effect of the forging pressure on the microstructure and residual stress development in Ti–6Al–4V linear friction welds. Acta Mater 2009;57:5582–92.
[39] Li W, Ma T, Zhang Y, Xu Q, Li J, Yang S, et al. Microstructure characterization and mechanical properties of linear friction welded Ti–6Al–4V alloy. Adv Eng Mater 2008;10:89–92.
[40] Ding R, Guo ZX, Wilson A. Microstructural evolution of a Ti–6Al–4V alloy during thermomechanical processing. Mater Sci Eng A 2002;327:233–45.
[41] Seshacharyulu T, Medeiros SC, Frazier WG, Prasad YVRK. Microstructural mechanisms during hot working of commercial grade Ti–6Al–4V with lamellar starting structure. Mater Sci Eng A 2002;325:112–25.
[42] Lutherjering G, Williams JC. Titanium. 2nd ed. Berlin Heidelberg New York: Springer; 2007.
[43] Askeland D, Phule P. The science and engineering of materials. 5th ed. London: Thomson; 2006.
[44] Fan XG, Yang H. Internal-state-variable based self-consistent constitutive modeling for hot working of two-phase titanium alloys coupling microstructure evolution. Int J Plast 2011;27:1833–52.
[45] Sheppard T, Norley J. Deformation characteristics of Ti–6AI–4V. Mater Sci Technol 1988;4:903–8.
[46] Ahmed T, Rack HJ. Phase transformations during cooling in α+β titanium alloys. Mater Sci Eng A 1998;243:206–11.
[47] Guo Y, Chiu Y, Attallah M, Li H. Characterization of dissimilar linear friction welds of ALPHA + BETA titanium alloys. J Mater Eng Perform 2012;21:770–6.

2014-11-03

Modelling the influence of the process inputs on the removal of surface contaminants from Ti-6Al-4V linear friction welds

McAndrew, Anthony

Elsevier

McAndrew, A.R., Colegrove, P.A., Addison, A.C. et al., 2014. Modelling the influence of the process inputs on the removal of surface contaminants from Ti-6Al-4V linear friction welds. Materials and design, Volume 66, part A, February 2015, pp.183-195

https://dx.doi.org/10.1016/j.matdes.2014.10.058